5 Materials Science

5-1 Room-temperature Ferroelectricity in Co-crystals of Nonpolar Organic Molecules

Ferroelectrics have attracted considerable interest from the viewpoint of practical applications in electronics and optics, for example capacitors, nonvolatile memory, high-performance gate insulators in FETs, piezoelectric elements, actuators, and nonlinear optics. Therefore, the development of organic ferroelectrics which can realize these excellent functions flexibly in the form of lightweight materials has been desired. Among the already known organic solid ferroelectrics, the most widely studied research targets are the ferroelectric polymers [1], such as vinylydene fluoride. In search for excellent ferroelectric properties, further material design and synthesis should be examined. In particular, low-molecular-weight organic ferroelectrics are virtually unexplored except for a few substances of polar molecules such as thiourea [2]. In this report, we describe new organic room-temperature ferroelectrics designed by a completely new approach implementing molecular compounds (co-crystals), in which two species of nonpolar molecules are bound by strong hydrogen bonding.

The new ferroelectrics are co-crystals of phenazine with chloranilic acid (Phz-H_2ca) and bromanilic acid (Phz-H_2ba), showing phase transitions at T_c = 253 K and 138 K, respectively. Fig. 1(a) shows the temperature dependence of dielectric constant ε for Phz-H_2ca, Phz-H_2ba, and their deuterated co-crystals. The dielectric constant ε at room temperature exceeds 100 for Phz-H_2ca and at T_c along the polar *b* axis reaches huge values (2000-3000) much larger than is observed in other organic ferroelectrics [3]. Furthermore, room-temperature ferroelectricity, an important property for applications especially as memory, has been successfully realized by deuteration of the hydrogen bonds [4]. For both anilic acids the increment of T_c is more than 50 K, and the highest T_c = 304 K of deuterated chloranilic acid (D_2ca) exceeds room temperature.

All of the Phz co-crystals studied show characteristic hysteresis below T_c in the polarization (*P*) versus electric field (*E*) curves. Fig. 1(b) shows *P*-*E* curves for Phz-D_2ca at various temperatures. The appearance of hysteresis below T_c = 304 K is direct evidence of ferroelectricity at room temperature. At 288 K, the remanent polarization P_r is ~ 0.6-0.7 μC/cm^2, and the coercive field of 0.5 kV/cm remains lower by 2-3 orders of magnitude than for typical ferroelectric polymers [1]. The low coercive field is advantageous from the point of view of device applications such as memory, because of the low operating-voltage required.

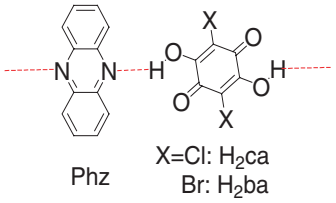

Phz

X=Cl: H_2ca
Br: H_2ba

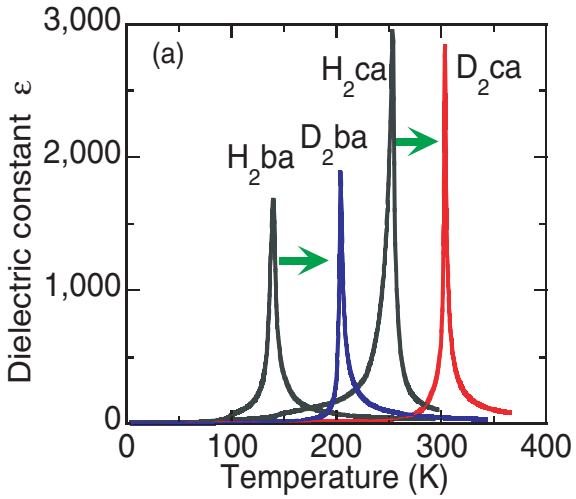

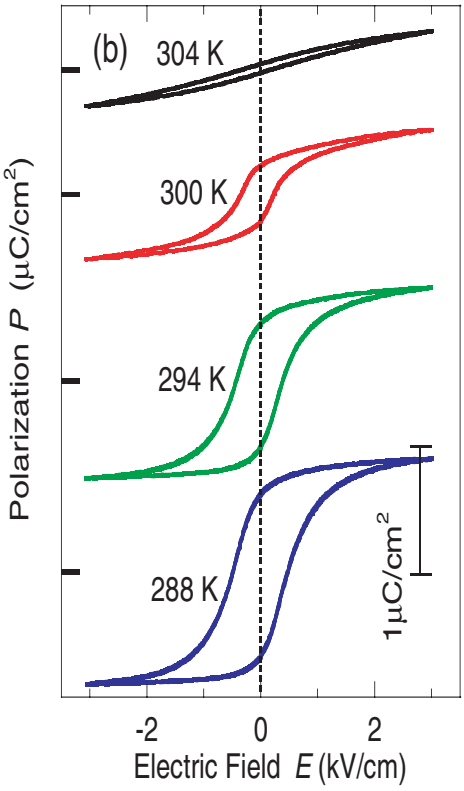

Figure 1
(a) Temperature dependence of the dielectric constant of Phz-H_2ca, Phz-H_2ba, and their deuterated co-crystals. An ac field (f =1 MHz) is applied along the polar (crystallographic *b*) axis parallel to the molecular stack. (b) Hysteresis loops of electric polarization at various temperatures for the Phz-D_2ca crystal.

To make clear the origin of the ferroelectricity, the crystal structure of the co-crystal has been determined in a Si-double-crystal monochromated synchrotron radiation (λ = 0.6869 Å) X-ray experiment [5]. A diffraction experiment was performed using an image plate system (Rigaku SPD) installed at BL-1A. In the ferroelectric co-crystals, intermolecular hydrogen bonding between the hydroxy groups of the acids and the nitrogen atoms of Phz gives rise to infinite chains of alternating acid and base molecules, as illustrated with dotted lines in Fig. 2(a). The protons of the acid are not transferred to the base, so both the component molecules remain neutral. It should be noted that the ferroelectric crystals studied here with large ε and P_r are made up from nonpolar neutral molecules. Each molecule constructs a uniform π-molecular stack along the crystallographic *b* axis. In the high-temperature paraelectric phase, the crystal structure is centrosymmetric (space group $P2_1/n$) with each molecule located at an inversion center. Below T_c, the crystal structure is asymmetric (space group $P2_1$), and consistent with the uniaxial ferroelectricity along the crystallographic *b* axis.

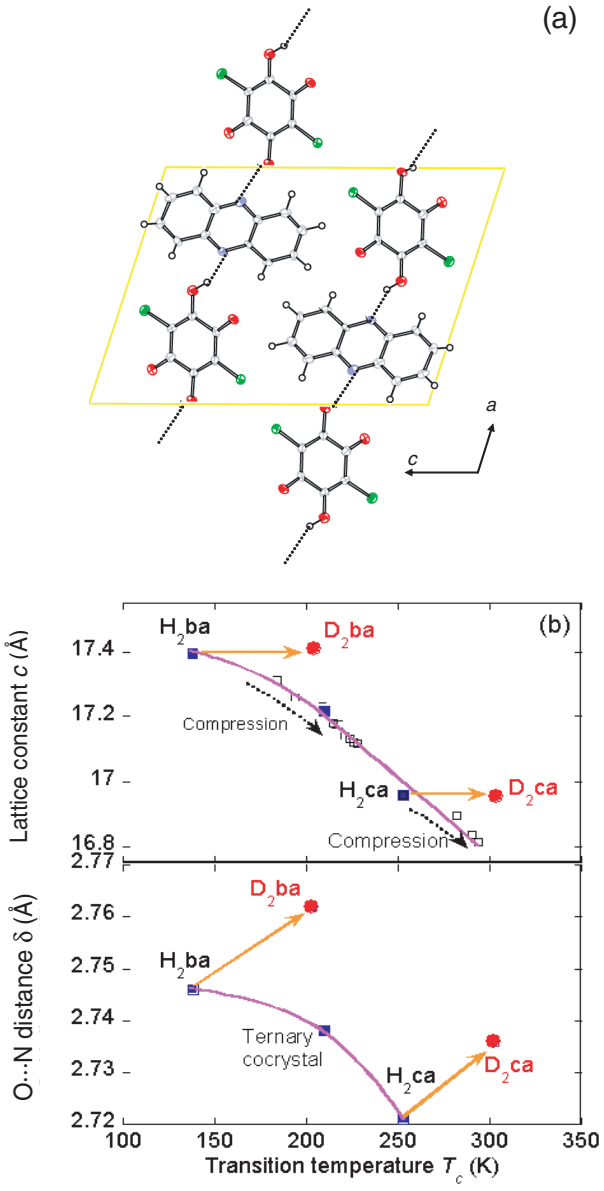

Figure 2
(a) Crystal structure of the ferroelectric co-crystal Phz-H_2ca in the low temperature phase. (b) Relation between T_c and structural changes (lattice parameter *c* (upper panel) and O•••N atomic distance δ(lower panel)) under hydrostatic pressure or upon deuteration.

The present findings of an extremely large isotope effect despite small lattice parameter changes (see Fig. 2(b), upper panel) indicate the critical role of the hydrogen bonds on the ferroelectricity in the co-crystals. We have also examined the way in which T_c depends on the hydrogen-bonding geometry (O•••N atomic distance δ), as shown in Fig. 2(b) (lower panel). The changes upon H/D substitution (δ↑, T_c↑) are in agreement with the general observation in hydrogen-bonded ferro-/antiferro-electrics having double-well proton potentials. However, chemical Cl/Br substitution in the anilic acids has an opposite effect (δ↑, T_c↓). Therefore, the observed large isotope effect cannot be explained simply by the geometric change of the hydrogen bonds.

The present approach is expected to be applicable to the development of organic ferroelectrics with improved performance and functions with further detailed studies .

R. Kumai[1], S. Horiuchi[1], Y. Tokura[1-3] ([1]AIST-CERC, [2]ERATO-SSS, [3]Univ. of Tokyo)

References

[1] T. Furukawa, *Phase Trans.*, **18** (1989) 143.
[2] J. Sworakowski, *Ferroelectrics*, **128** (1992) 295.
[3] S. Horiuchi, F. Ishii, R. Kumai, Y. Okimoto, H. Tachibana, N. Nagaosa and Y. Tokura, *Nature Materials.*, **4** (2005) 163.
[4] S. Horiuchi, R. Kumai and Y. Tokura, *J. Am. Chem. Soc.*, **127** (2005) 5010.
[5] Phz-H_2ca (295 K), $C_{18}H_{10}Cl_2N_2O_3$: Monoclinic $P2_1/n$, a = 12.399(2) Å, b = 3.8533(7) Å, c = 16.957(2) Å, β = 107.890(6)°, V = 771.0(2) Å^3, R = 0.048, R_W = 0.050 for 3150 independent reflections ($|Fo| > 3\sigma(|Fo|$, $2\theta_{max}$ = 80.15°) and 124 variable parameters. Phz-H_2ca (160 K), $C_{18}H_{10}Cl_2N_2O_3$: Monoclinic $P2_1$, a = 12.422(2) Å, b = 3.7909(3) Å, c = 16.954(3) Å, β = 107.844(3)°, V = 761.1(2) Å^3, R = 0.050, R_W = 0.054 for 1728 independent reflections ($|Fo| > 3\sigma(|Fo|$, $2\theta_{max}$ = 50.7°) and 247 variable parameters.

5-2 Formation of Ice Nanotubes inside Carbon Nanotubes

It is well known that the physical properties of water are almost independent of volume, changing only gradually in the bulk scale region. When the volume decreases below the few-molecule size, however, water exhibits quite different properties compared to the bulk scale. Such waters exist everywhere on earth and play important roles in the occurrence of various phenomena. Recently, we have found that water confined inside single-walled carbon nanotubes (SWCNTs) with one-dimensional hollow cavities of diameters of 8 to 12 Å displays interesting structural properties [1,2] which cannot be extrapolated from the macroscopic scale.

Diameter-controlled SWCNT samples were examined by means of detailed X-ray diffraction (XRD) structural analysis conducted at BL-1B. Fig. 3 shows the typical temperature dependence of the XRD patterns from an SWCNT sample. It was found that water was easily adsorbed inside the SWCNTs at room temperature, and a new form of ice, "ice nanotubes" (ice-NT) was formed at lower temperatures. Fig. 4 illustrates one example of the observed ice-NT structures, pentagonal ice-NT, where the water molecules form *n*-membered rings, through hydrogen bonds. (Here *n* represents an integer.) These rings stack one-dimensionally to form *n*-membered ice-NTs inside the SWCNT. While the possibilty of ice-NT formation was predicted by Koga *et al.* in 2001 using molecular dynamics calculations for water confined inside SWCNT by axial pressures of 50 to 500 MPa [3], the present experiments show that ice-NTs can be formed without applying high pressures.

With increasing SWCNT diameter, ice-NTs with larger *n* were more preferentially formed. It was also found that the melting point of the ice-NTs varies greatly depending on the SWCNT diameter, with smaller diameters leading to higher melting points. This is contrary to existing empirical rules (see Fig. 5). In particular, water in SWCNTs with diameters of 11.7 Å was found to crystallize at 300 K or lower. In other words, we have succeeded in forming the first room-temperature ice-NTs at pressures below 0.1 MPa (1 atm). Moreover, we have discovered that the water inside an SWCNT vaporizes at around 320 K and is subsequently ejected, leading to the possibility of a number of applications, including nano-size inkjet printing.

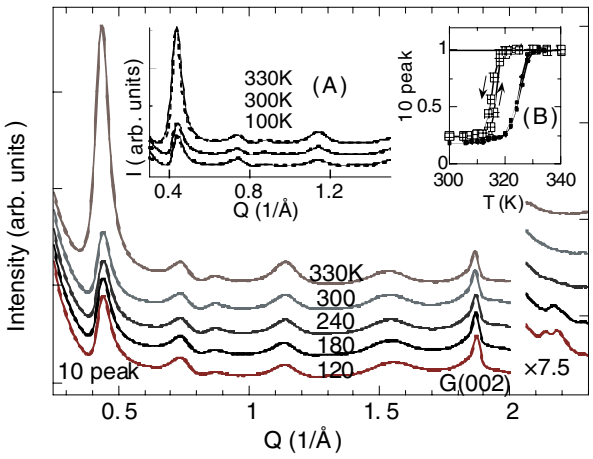

Figure 3
Temperature dependence of the XRD patterns of a SWCNT sample with an average diameter of 13.5 Å. The small peaks at Q~2.2Å^{-1} are assigned to the ice-NTs. The peaks denoted with G(002) are due to graphite-like impurities. Inset (A): Comparison of the observed and simulated XRD patterns after background-removal. Inset (B): Temperature dependences of the 10 peak intensity at Q~0.45 Å^{-1} for two SWCNT samples with different diameters. The larger and smaller squares are for 13.5 and 11.7 Å diameter SWCNT samples, respectively. The steep decreases below around 320 K are evidence for the adsorption of water inside the SWCNTs.

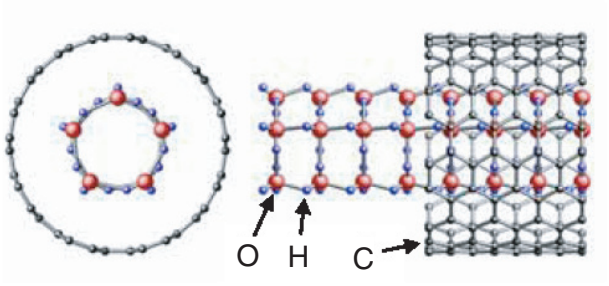

Figure 4
A schematic illustration of pentagonal (5-membered) ice-NT formed inside an SWCNT. The melting point is 300K.

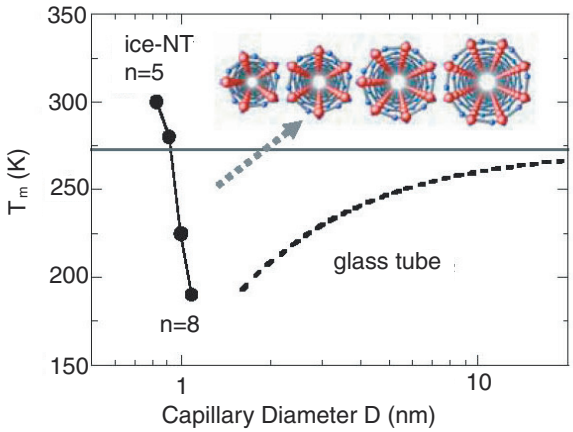

Figure 5
The melting point of ice-NT as a function of the cavity diameter of the SWCNT. The dashed line is the melting point of water confined inside a glass tube extrapolated from the bulk region. The inset shows schematic views of 5 to 8-membered ice-NTs, looking along the tube-axis.

Y. Maniwa[1,3], H. Kataura[2], M. Abe[1], A. Udaka[1], S. Suzuki[1], Y. Achiba[1], H. Kira[1], K. Matsuda[1], H. Kadowaki[1] and Y. Okabe[1] ([1]Tokyo Metropolitan Univ., [2]Nanotech. Res. Inst., [3]CREST)

References

[1] Y. Maniwa, H. Kataura, M. Abe, S. Suzuki, Y. Achiba, H. Kira and K. Matsuda, *J. Phys. Soc. Jpn.*, **71** (2002) 2863.
[2] Y. Maniwa, H. Kataura, M. Abe, A. Udaka, S. Suzuki, Y. Achiba, H. Kira, K. Matsuda, H. Kadowaki and Y. Okabe, *Chem. Phys. Lett.*, **401**, (2005) 534.
[3] K. Koga, G. T. Gao, H. Tanaka and X. C. Zeng, *Nature,* **412** (2001) 802.

5-3 Preferred Location of the Metal Ions in the Minor Isomers of M@C_{82}

The location of the metal ions is an important problem in the study of endohedral metallofullerenes because this, along with the cage symmetries, is closely associated with the overall electronic properties [1]. The major and minor isomers of metal endohedral C_{82}, M@C_{82}, have been named as isomers I and II, as distinguished by their retention times in high-performance liquid chro-

matography studies used for the separation of isomers. The molecular symmetries of isomers I and II have been determined to be C_{2v} and C_s [2,3]. Analyses using maximum entropy methods (MEM) and Rietveld refinements for isomer-I of Y@C_{82} and Sc@C_{82} showed that the metal ions were located at off-center positions near the hexagon rings of the C_{2v}-C_{82} cage [4,5]. A subsequent EXAFS analysis for the major isomer of Dy@C_{82} also showed that the Dy ion lay near to the hexagon ring of the cage [6]. In the present study, we have studied Dy L_{III}-edge EXAFS for the minor isomer of Dy@C_{82} to determine the location of the Dy ion inside the cage.

A pure sample of the Dy@C_{82} isomer II was obtained using a method reported elsewhere [6]. A solvent-free powder sample of this isomer was introduced into a polyethylene bag for EXAFS without exposure to air in an Ar glove box, and the Dy L_{III}-edge EXAFS was recorded at 300 K in the fluorescence mode with a Si(111) monochromator at BL-12C. The EXAFS oscillation, $\chi(k)$ was extracted from the Dy L_{III}-edge fluorescence excitation spectrum, and the radial distribution function, $\phi(r)$ was obtained by Fourier transform of $k^3\chi(k)$ in the k-region of 2.0 – 10.5 Å^{-1}. Three pronounced peaks were observed in the imaginary part of $\phi(r)$, at 1.95, 2.32 and 2.68 Å, as shown in Fig. 6. These peaks can be assigned to scattering between the Dy atom and the nearest C atoms: the first nearest, C(1), second nearest, C(2), and third nearest, C(3). The local structure around the Dy ion was determined by least-squares fitting for the $\chi(k)$ obtained by an inverse-Fourier transform of $\phi(r)$; the fitting was performed based on the model that the Dy ion was placed near the fused bond between two hexagon rings in the C_s(c)-C_{82} cage, as has been suggested by a theoretical prediction (Fig. 7). The coordination numbers of the C(1), C(2), and C(3) atoms were 2, 8 and 4, as shown in Fig. 7. The real distances, $r_{Dy\text{-}C(1)}$, $r_{Dy\text{-}C(2)}$ and $r_{Dy\text{-}C(3)}$, were determined to be 2.347(2), 2.746(6) and 3.184(6) Å, by parameter fitting of $\chi(k)$ over the range 2.5 – 10.0 Å^{-1} as obtained from an inverse-Fourier transform of $\phi(r)$ over the range r = 1.43 – 3.03 Å, and the final R factor was found to be 2.1%. When the Dy ion was placed at a position separated from C(1) by 2.35 Å inside the C_s(c)-C_{82} cage,

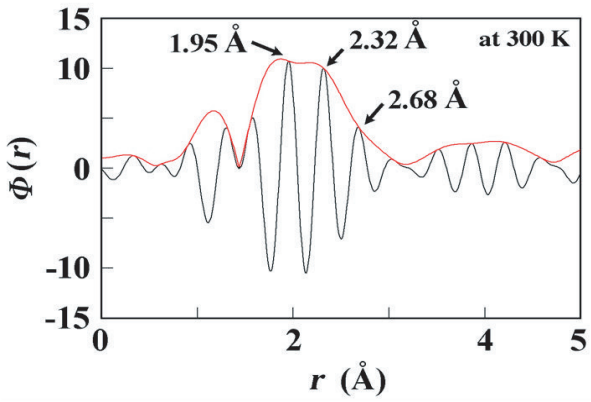

Figure 6
Absolute (red) and imaginary (black) parts of $\Phi(r)$ obtained from the Fourier-transform of $k^3\chi(k)$.

the $r_{Dy\text{-}C(2)}$ and $r_{Dy\text{-}C(3)}$ values can be predicted to be 2.73 and 3.08 Å, respectively. These values are consistent with the experimental values determined by EXAFS. This implies that the structure determined by EXAFS based on this model is a reasonable model for the structure of the minor isomer. Furthermore, the EXAFS data was also analyzed based on the model that the Dy ion was located on the hexagon ring, but the experimental data could not be reproduced with this model. Consequently, it can be concluded that the Dy ion is located near the fused bond between two hexagon rings.

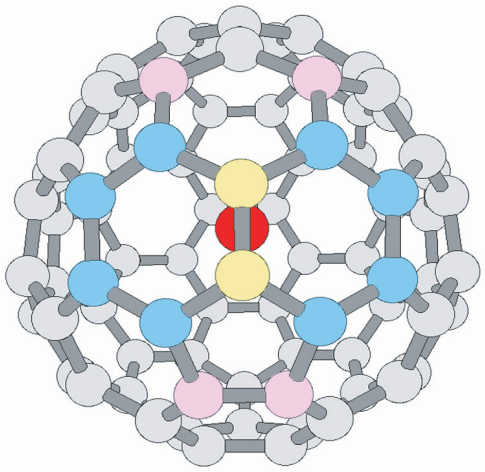

Figure 7
Model structures of C_s-Dy@C_{82} with Dy ions placed near the center of the fused bond. The red, yellow, blue and pink circles refer to the Dy ion, C(1), C(2) and C(3), respectively.

Y. Kubozono[1,2] and Y. Takabayashi[3] ([1]Okayama Univ., [2]CREST, [3]Univ. of Durham)

References

[1] S. Nagase, K. Kobayashi, T. Kato and Y. Achiba, *Chem. Phys. Lett.,* **201** (1993) 475.
[2] T. Akasaka, T. Wakahara, S. Nagase, K. Kobayashi, M. Waelchli, K. Yamamoto, M. Kondo, S. Shirakura, S. Okubo, T. Maeda, T. Kato, M. Kako, Y. Nakadaira, R. Nagahata, X. Gao, E.V. Caemelbecke and K. M. Kadish, *J. Am. Chem. Soc.*, **122** (2000) 9316.
[3] T. Akasaka, T. Wakahara, S. Nagase, K. Kobayashi, M. Waelchli, K. Yamamoto, M. Kondo, S. Shirakura, Y. Maeda, T. Kato, M. Kako, Y. Nakadaira, X. Gao, E. V. Caemelbecke and K. M. Kadish, *J. Phys. Chem. B,* **105** (2001) 2971.
[4] M. Takata, B. Umeda, E. Nishibori, M. Sakata, Y. Saito, M. Ohno and H. Shinohara, *Nature,* **377** (1995) 46.
[5] E. Nishibori, M. Takata, M. Sakata, M. Inakuma and H. Shinohara, *Chem. Phys. Lett.,* **298** (1998) 79.
[6] S. Iida, Y. Kubozono, Y. Slovokhotov, Y. Takabayashi, T. Kanbara, T. Fukunaga, S. Fujiki, S. Emura and S. Kashino, *Chem. Phys. Lett.*, **338** (2001) 21.

5-4 Positronium Time-of-flight Spectroscopy from a Porous Dielectric Film

The need of the semiconductor industry to reduce signal delays, cross talk and energy dissipation in future ultra-large integrated circuits (ULSI) promotes research

on porous interlayer dielectrics with reduced dielectric constants. Positronium (Ps) is well documented as a powerful probe for nanometer-scale pores in various materials. In this study we have observed Ps emission from a porous low dielectric constant film through open pores using Ps time-of-flight (Ps TOF) spectroscopy at KEK slow positron facility.

A porous film with a thickness of about 400 nm was prepared from silica monomers by spin coating and subsequent baking/curing processes at elevated temperatures. The relative dielectric constant of the film was about 2.3, much lower than that for nonporous SiO_2 (4.5). Ps TOF experiments were carried out with the setup described elsewhere [1,2]. The output pulses from a photomultiplier tube corresponding to the detection of positron annihilation photons were recorded with a fast digital oscilloscope (DSO). The waveforms were then digitized and stored in the memories of the DSO.

The waveforms were smoothed and traced one by one using a personal computer. Signals irrelevant to positron annihilation were removed by eliminating pulses with amplitudes lower than a critical level, set by carrying out a pulse-height distribution analysis of all the waveforms. After the elimination of these low amplitude pulses, a TOF spectrum was obtained by creating a frequency distribution as a function of the time difference between the accelerator trigger and the detection of an annihilation photon by the scintillator.

Fig. 8 shows a comparison of Ps TOF spectra for the porous film at different flight lengths (z) before and after the data processing mentioned above. The incident positron energy was 0.5 keV. The spectra obtained after the data processing have a better time resolution of about 23 ns full-width at half-maximum (fwhm) and show clearer TOF signals (free from distortion and wiggles) than those obtained by simple averaging on the DSO. The validity of the spectra obtained after processing is further confirmed by the excellent proportionality between the TOF peak location and flight length in Fig. 9. From the relationship in Fig. 9 the Ps emission energy was determined to be 1.8 eV.

It was possible to observe TOF peaks from the porous film using incident positron energies of up to 4.0 keV, corresponding to a mean positron implantation depth larger than 200 nm. This result indicates that Ps is emitted through open pores present in the film. Because of serious post-etch integration problems such as voiding and barrier metal intrusion caused by chemical contamination into open, connected pores, the control of open porosity is an important issue in the development of interlayer dielectrics. This study demonstrated the usefulness of Ps as a probe for *open* pores in thin films.

Y. Kobayashi[1], K. Ito[1], K. Hirata[1], K. Sato[2], R. S. Yu[3] and T. Kurihara[4] ([1]AIST, [2]Tokyo Gakugei Univ., [3]JAERI, [4]KEK-PF)

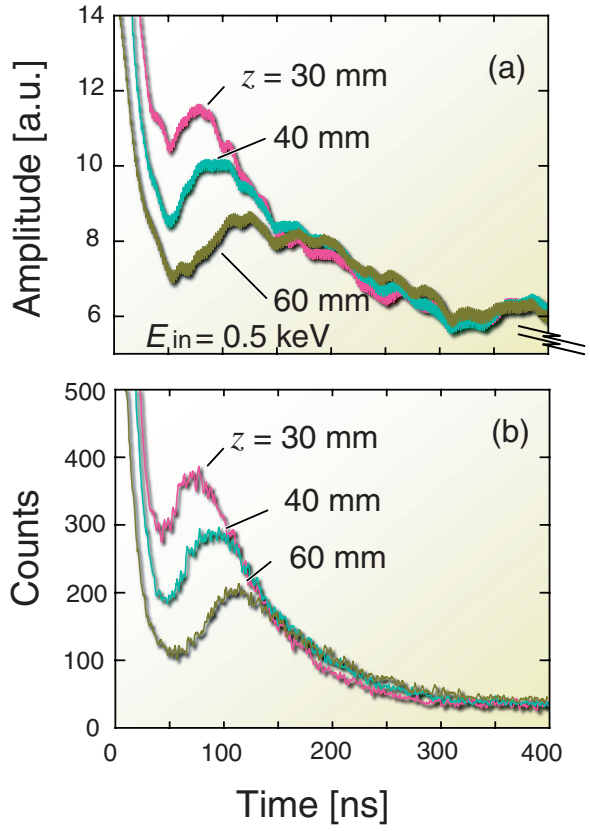

Figure 8
Ps TOF spectra for a 400 nm thick porous film at different flight lengths before (a) and after (b) data processing.

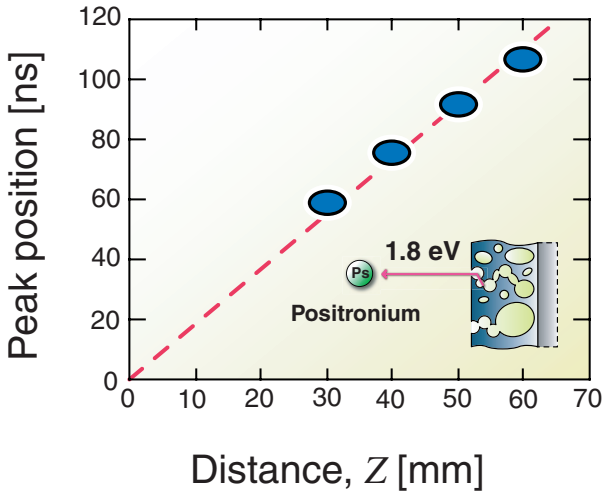

Figure 9
Plot of the Ps TOF peak location versus flight length.

References

[1] T. Kurihara, A. Yagishita, A. Enomoto, H. Kobayashi, T. Shidara, A. Shirakawa, K. Nakahara, H. Saitou, K. Inoue, Y. Nagashima, T. Hyodo, Y. Nagai, M. Hasegawa, Y. Inoue, Y. Kogure and M. Doyama, *Nucl. Instrm. Methods in Phys. Res. B*, **171** (2000) 199.

[2] T. Kurihara, Y. Nagashima, T. Shidara, H. Nakajima, S. Ohsawa, M. Ikeda, T. Oogoe, K. Kakihara, Y. Ogawa, A. Shirakawa. K. Furukawa, T. Sanami and A. Enomoto, *Materials Science Forum*, **486** (2004) 445.